ADVANCED MATERIALS
www.advmat.de

Halide Heterogeneous Structure Boosting Ionic Diffusion and High-Voltage Stability of Sodium Superionic Conductors

Jiamin Fu, Shuo Wang, Duojie Wu, Jing Luo, Changhong Wang, Jianwen Liang, Xiaoting Lin, Yang Hu, Shumin Zhang, Feipeng Zhao, Weihan Li, Minsi Li, Hui Duan, Yang Zhao, Meng Gu, Tsun-Kong Sham,* Yifei Mo,* and Xueliang Sun**

The development of solid-state sodium-ion batteries (SSSBs) heavily hinges on the development of an superionic Na^+ conductor (SSC) that features high conductivity, (electro)chemical stability, and deformability. The construction of heterogeneous structures offers a promising approach to comprehensively enhancing these properties in a way that differs from traditional structural optimization. Here, this work exploits the structural variance between high- and low-coordination halide frameworks to develop a new class of halide heterogeneous structure electrolytes (HSEs). The halide HSEs incorporating a UCl_3-type high-coordination framework and amorphous low-coordination phase achieves the highest Na^+ conductivity (2.7 mS cm^{-1} at room temperature, RT) among halide SSCs so far. By discerning the individual contribution of the crystalline bulk, amorphous region, and interface, this work unravels the synergistic ion conduction within halide HSEs and provides a comprehensive explanation of the amorphization effect. More importantly, the excellent deformability, high-voltage stability, and expandability of HSEs enable effective SSSB integration. Using a cold-pressed cathode electrode composite of uncoated $Na_{0.85}Mn_{0.5}Ni_{0.4}Fe_{0.1}O_2$ and HSEs, the SSSBs present stable cycle performance with a capacity retention of 91.0% after 100 cycles at 0.2 C.

1. Introduction

Given the growing scarcity of lithium resources, solid-state sodium-ion batteries (SSSBs) have garnered significant attention owing to their sustainable composition, high theoretical energy density, and inherent safety advantages.[1] However, the development of solid-state sodium-ion batteries (SSSBs) imposes stringent requirements on superionic Na-ion conductors (SSCs), including high ionic conductivity (>1 mS cm^{-1}) at room temperature (RT), excellent deformability for intimate solid-solid contact, and exceptional interfacial stability with electrode materials, yet no single SSC currently fulfills all these requirements simultaneously.[2] Among the several categories of SSCs, inorganic oxide SSCs[3] show higher Na-ion conductivity of ≈1 mS cm^{-1} and better electrochemical stability than those of polymer-based SSCs, but their rigid nature makes them extremely challenging to maintain tight

J. Fu, J. Luo, J. Liang, X. Lin, Y. Hu, S. Zhang, F. Zhao, W. Li, M. Li, H. Duan, Y. Zhao, X. Sun
Department of Mechanical and Materials Engineering
University of Western Ontario
London, ON N6A 5B9, Canada
E-mail: xsun@eng.uwo.ca

J. Fu, T.-K. Sham
Department of Chemistry
University of Western Ontario
London, ON N6A 5B7, Canada
E-mail: tsham@uwo.ca

The ORCID identification number(s) for the author(s) of this article can be found under https://doi.org/10.1002/adma.202308012

DOI: 10.1002/adma.202308012

S. Wang, Y. Mo
Department of Materials Science and Engineering
University of Maryland
College Park, MD 20742, USA
E-mail: yfmo@umd.edu

D. Wu, C. Wang, M. Gu, X. Sun
Eastern Institute for Advanced Study
Eastern Institute of Technology
Ningbo, Zhejiang 315200, P. R. China
E-mail: m.danny.gu@gmail.com

D. Wu, M. Gu
Department of Materials Science and Engineering
Southern University of Science and Technology
Shenzhen 518055, China

interparticle contact in SSSBs.[1a] Although closo-borates,[4] sodium thiophosphates,[5] and their analogues[6] are emerging in recent years due to their deformability and exceptional ionic conductivity (up to the level of 10 mS cm^{-1}), the limited oxidative stability hinders their integration with high-voltage cathodes for competitive energy densities.

Recently, the successful discovery of a range of halide-based Li-ion conductors,[7] which exhibit good deformability, high ionic conductivity, and (electro)chemical stability, has inspired research into sodium halide analogues as potential SSCs. However, due to the disparity in ionic radius between Li (76 pm) and Na (>100 pm), the design principles for superionic lithium conductors cannot be directly applied to SSCs. As a result, the reported halide-based SSCs generally exhibit insufficient ionic conductivity. For instance, the trigonal structured Na_2ZrCl_6[8] and its aliovalently substituted $Na_{3-x}Er_{1-x}Zr_xCl_6$[9] and $Na_{3-x}Y_{1-x}Zr_xCl_6$[10] present Na^+ conductivities of 0.018 mS cm^{-1} (30 °C), 0.04 mS cm^{-1} (25 °C), and 0.066 mS cm^{-1} (20 °C), respectively. Ridley et al.[11] further demonstrated an increased RT ionic conductivity of $Na_xY_{0.25}Zr_{0.75}Cl_{3.75+x}$ to 0.4 mS cm^{-1} by reducing the NaCl content and transitioning to an amorphous state. The authors suggest that the bigger free volume and higher number of Na^+ vacancies in the amorphous state likely account for the high ionic conductivity. However, no halide SSC has achieved an ionic conductivity above 1 mS cm^{-1} as comparable to the lithium analogues.

The construction of heterogeneous structures offers an alternative approach to enhancing ion conduction distinct from traditional structural optimization.[12] Hiram Kwak et al.[13] recently reported an intriguing finding of improving the Na^+ conductivity of 0.011 mS cm^{-1} for Na_2ZrCl_6 to 0.11 mS cm^{-1} for ZrO_2-Na_2ZrCl_6 even if the bulk ZrO_2 is not conductive. Similarly, an increase in ionic conductivity by one to two orders of magnitude has frequently been observed in various heterostructure systems, such as crystal-crystal ($LiI{\cdot}Al_2O_3$,[14] $LiI{\cdot}Li_3PO_4$,[15] and $Li_2ZrCl_6{\cdot}ZrO_2$[13]), crystal-glass ($AgI{\cdot}Ag_3BO_3$,[16] $P_2S_5{\cdot}Li_2S{\cdot}LiI$,[17] and $LiBH_4$·fumed silica[18]), and polymer-inorganic (PEO·Al_2O_3[19] and PEO·$Li_7La_3Zr_2O_{12}$[20]), which are usually attributed to the effect of space charge layer at the interface.[12] However, the exploration of halide-based heterogeneous structure electrolytes (HSE) as potential SSCs is still on the way, and there remains a lack of clarity regarding the specific roles of heterogeneous components on ionic conductivity.

Besides the common close-packed anion structures of Li^+ superionic conductors, we have lately proposed another group of UCl_3-type frameworks,[21] in which highly distorted octahedral sites constitutes a fast one-dimensional (1D) diffusion channel for Li^+/Na^+ hopping. However, the limitation of 1D transport characteristics restricts its macroscopic ionic conductivity across mismatched grains. Yin et al.[22] take advantage of high-valence cationic doping to obtain three-dimensional (3D) transport within the single structure, leading to a high Li^+ ionic conductivity of 3.02 mS cm^{-1} at 30 °C. When the UCl_3-type lattice maintains the fast 1D channels without aliovalent substitution, we found that the UCl_3-type lattice possesses an appealing capability to induce amorphization in surrounding low-coordination halides, creating interparticle conduction buffers to achieve fast macroscopic ion diffusion.[21] These behaviors fulfill the key focuses of HSEs development, including the sustained structural integrity of each component and fast ion diffusion in the different components. Hence, incorporating UCl_3-type frameworks into halide HSEs represents a promising strategy for effectively exploiting the rapid 1D diffusion and amorphization capabilities inherent to the UCl_3-type framework, thereby enhancing Na^+ ion conductivity synergistically.

In this study, we delve into the structural characteristics of polycationic halides that incorporate the UCl_3-type frameworks and different ternary metal halides. By exploiting the structural variances between high- and low-coordination halide frameworks, we have developed a novel class of halide HSEs that exhibit an outstanding ionic conductivity of up to 2.7 mS cm^{-1}. This achievement marks the highest value recorded among halide SSCs to date. The heterogeneous interactions within the HSEs were characterized by X-ray diffraction (XRD), pair distribution function (PDF), high-resolution transmission electron microscopy (HRTEM), and extended X-ray absorption fine structure (EXAFS). By combining ab initio molecular dynamics (AIMD) simulations with low-temperature electrochemical impedance fittings, we clarified the individual contribution of the crystalline bulk, amorphous region, and interface to ionic conductivity. Notably, we distinctly highlighted the substantial role of the amorphization effect in this context. Furthermore, the halide HSEs demonstrated excellent deformability, high-voltage stability, and expandability. The cold-pressed cathode composite using uncoated $Na_{0.85}Mn_{0.5}Ni_{0.4}Fe_{0.1}O_2$ (NMNFO) and HSEs presented stable cycle performance with a capacity retention of 91.0% after 100 cycles at 0.2 C in SSSBs, outperforming the composite performance using Na_3PS_4 as catholyte. The composition of halide HSEs is highly designable and extendable, allowing for a tunable cathode–electrolyte interphase (CEI) design for different cathode materials and requirements.

2. Results and Discussion

2.1. Construction and Characterization of Halide Heterostructures

Two types of sodium metal ternary halides, categorized based on the distinct metal-halogen coordination numbers (C.N.), were mechanochemically synthesized in this study: 1) high coordination frameworks (HCF, C.N. > 6) represented by UCl_3-type $Na_{3x}M_{2-x}Cl_6$ (M = La, Sm) and 2) low coordination frameworks (LCF, C.N. ≤ 6) represented by dispersed $[MCl_6]^{x-}$ octahedra, such as $NaTaCl_6$ (LCF-Ta). **Figure 1**a,b presents the Rietveld refinements of XRD patterns of the HCF candidates, $Na_{0.75}Sm_{1.75}Cl_6$ (HCF-Sm) and $Na_{0.75}La_{1.75}Cl_6$ (HCF-La). HCF-Sm and HCF-La are constituted by $[MCl_9]^{6-}$ tricapped trigonal prism with Na atoms partially occupying Wyckoff sites *2b* (octahedral sites) and *2c* (La, Sm sites), as shown in Figure 1d. In the UCl_3-type structure, the AIMD simulations revealed fast Na^+ conduction in the numerous face-sharing distorted octahedra sites along the *c*-axis (Figure S1a,b, Supporting Information). As for an LCF candidate, according to the Rietveld refinements of XRD pattern (Figure 1c), the crystalline LCF-Ta comprises an $[TaCl_6]^-$ octahedral framework located at the corners of the unit cell ($P2_1/c$) edge-sharing by two $[NaCl_7]^{6-}$ capped trigonal prism (Figure 1e). Different from the UCl_3-type structure, Na^+ ions in

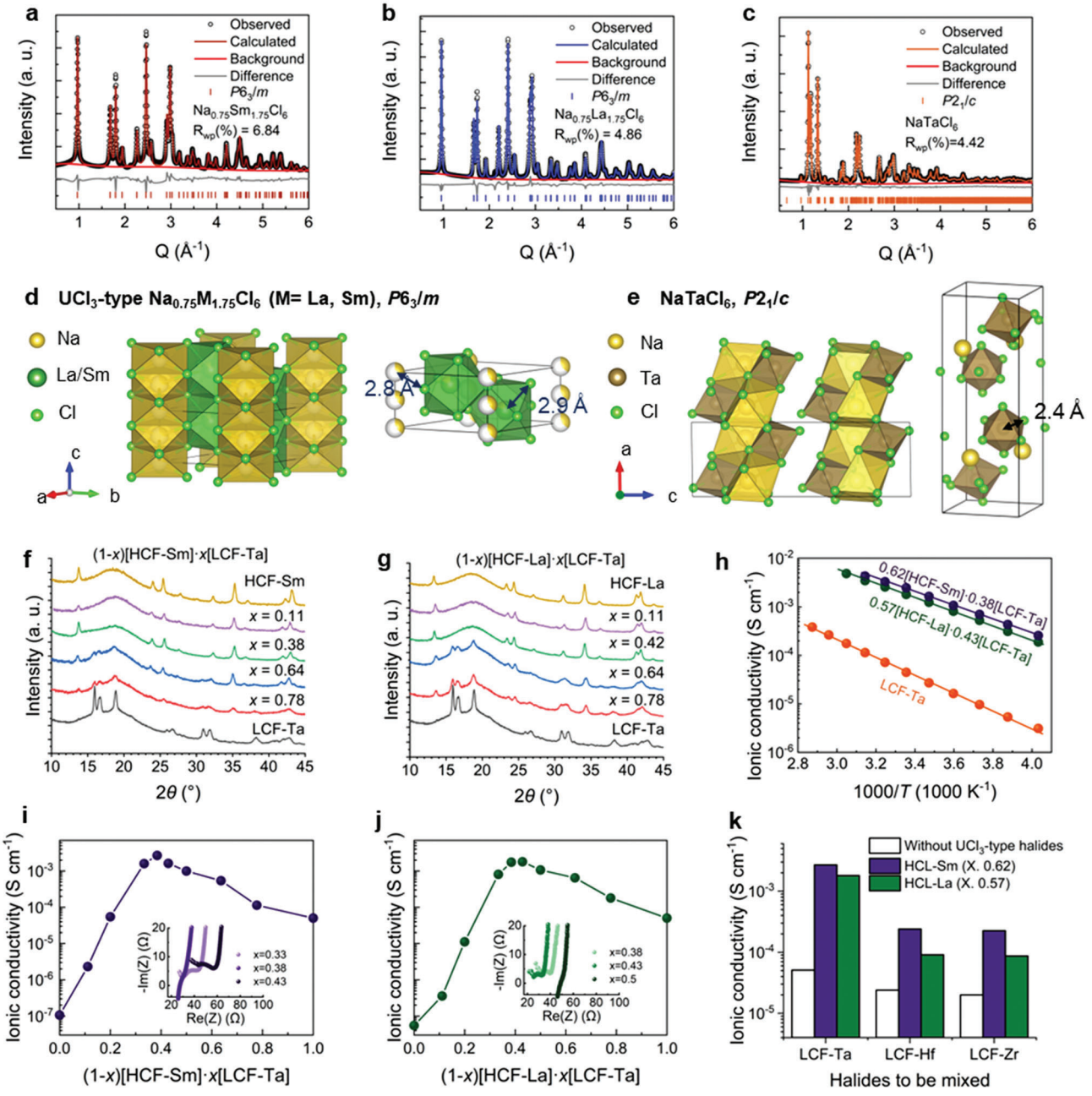

Figure 1. Characterization of HCF-Sm/La, LCF-Ta, and their heterogeneous composite. Synchrotron-based X-ray diffraction patterns (SXRD, $\lambda = 0.3497$ Å) and the Rietveld refinements of a) $Na_{0.75}Sm_{1.75}Cl_6$ (HCF-Sm), b) $Na_{0.75}La_{1.75}Cl_6$ (HCF-La), and c) $NaTaCl_6$ (LCF-Ta). d) The crystal structure of UCl_3-type $Na_{0.75}M_{1.75}Cl_6$ (M = La, Sm). e) The crystal structure of $NaTaCl_6$. The XRD patterns ($\lambda = 1.5406$ Å, Cu K_α) of composites of LCF-Ta with f) HCF-Sm as (1-x)[HCF-Sm]·x[LCF-Ta] and g) HCF-La as (1-x)[HCF-La]·x[LCF-Ta]. h) Arrhenius plots of the LCF-Ta, 0.62[HCF-Sm]·0.38[LCF-Ta], and 0.57[HCF-La]·0.43[LCF-Ta]. The ionic conductivities of i) (1 − x)[HCF-Sm]·x[LCF-Ta] and j) (1 − x)[HCF-La]·x[LCF-Ta] at 25 °C. k) The ionic conductivities of HSEs based on 0.62[HCF-Sm]·0.38LCF and 0.57[HCF-La]·0.43LCF using different LCFs.

LCF-Ta are confined at equilibrium sites surrounding by orderly distributed $[TaCl_6]^-$ octahedra as depicted in AIMD simulations (Figure S1c, Supporting Information). The formation of a 3D diffusional network in LCF-Ta requires overcoming a substantial activation energy barrier, which gives rise to an experimental Na^+ conductivity of 5.0×10^{-2} mS cm^{-1}. In contrast, the 1D diffusion of HCF-Sm and HCF-La hinders macroscopic percolation due to lattice mismatching between polycrystalline and results in low experimental Na^+ conductivities of 1.1×10^{-4} and 5.5×10^{-5} mS cm^{-1} at RT (Figure S1d–f, Supporting Information), respectively. Both types of Na-based halide materials currently have their limitations, leading to low apparent ionic conductivities. Following Pauling's rules for ionic compounds, the cation–anion radius ratio r^+/r^- determines the C.N. of the cation and the stability

of the cation within the coordinated polyhedron of anions. Therefore, the dissolution of $[SmCl_9]^{6-}$ and $[TaCl_6]^-$ into each other becomes challenging. A combination of the two shall likely form a heterogeneous structure rather than a solid solution, thus fully utilizing the fast 1D Na^+ diffusion in UCl_3-type HCFs and their capability of inducing amorphization.

The optimal composition and synthesis conditions of halide HSEs between HCF and LCF were investigated. The diffraction patterns of the heterostructures are shown in Figure 1f,g and Figure S2 (Supporting Information). As the LCF-Ta content decreases, the diffraction peaks become weaker, leading to a noticeable increase in the dominance of the HCF-Sm/HCF-La diffraction peaks. The resulting HSEs exhibit enhanced ionic conductivities (Figure 1h) and low activation energies (Figure S3, Supporting Information) compared with those of the individual LCF-Ta sample. As illustrated in Figure 1i,j, both in (1-x)[HCF-Sm]·x[LCF-Ta] and (1–x)[HCF-La]·x[LCF-Ta], the ionic conductivity is optimized within the range of x = 0.35–0.5. Notably, the composition of 0.62[HCF-Sm]·0.38[LCF-Ta] demonstrates an exceptional ionic conductivity of 2.7 mS cm^{-1} at 25 °C, while 0.57[HCF-La]·0.43[LCF-Ta] exhibits a comparable ionic conductivity of 1.8 mS cm^{-1} at 25 °C. These values represent the highest conductivities achieved to date compared to that of other reported halide SSCs (0.02–0.11 mS cm^{-1}). In addition, as proof of the generality of the halide HSE design, LCF-Ta was further replaced with Na_2ZrCl_6 (LCF-Zr) or Na_2HfCl_6 (LCF-Hf), respectively. The corresponding ionic conductivity also increased from the level of 0.01 mS cm^{-1} (pristine Na_2ZrCl_6 or Na_2HfCl_6) to the level of 0.1 mS cm^{-1} (for HSEs) as shown in Figure 1k. The SXRD observed similar sharp peaks from HCF-Sm/HCF-La and large bumps around $2\theta = 4°$ ($\lambda = 0.3497$ Å) from LCF-Zr/LCF-Hf (Figure S4a,b, Supporting Information), confirming the formation of heterostructures.

To investigate the structural characteristics of HSEs, we conducted SXRD and PDF measurements on 0.62[HCF-Sm]·0.38[LCF-Ta] and 0.57[HCF-La]·0.43[LCF-Ta], as depicted in **Figure 2**a,b. After heterogenized and synthesis of HSEs, the diffraction peaks relevant to LCF-Ta seem greatly quenched. Indeed, the crystalline LCF-Ta transforms into an amorphous state instead of forming a solid solution with HCF-Sm or HCF-La. The distribution of distances G(r) between pairs of atoms in 0.62[HCF-Sm]·0.38[LCF-Ta] and 0.57[HCF-La]·0.43[LCF-Ta] can be found in Figure 2c. The peak at approximately 2.4 Å characterizes the Ta-Cl distance in octahedron of LCF-Ta, and the peak at ≈2.8–2.9 Å characterizes the Sm/La-Cl distance in tricapped trigonal prisms of HCF-Sm/La. Both 0.62[HCF-Sm]·0.38[LCF-Ta] and 0.57[HCF-La]·0.43[LCF-Ta] present a mixed characteristic of $[TaCl_6]^-$ octahedron and $[MCl_9]^{6-}$ tricapped trigonal prisms (M = La, Sm), which confirms that 0.62[HCF-Sm]·0.38[LCF-Ta] and 0.57[HCF-La]·0.43[LCF-Ta] are a composite of crystalline HCF-Sm/HCF-La and amorphous LCF-Ta. Similarly, $[ZrCl_6]^{2-}$ or $[HfCl_6]^{2-}$ octahedrons have been identified in the PDF of HSEs using LCF-Zr or LCF-Hf (Figure S4c,d, Supporting Information). The "box-car fitting" was utilized to extract quantitative information about the length scale of local atomic order from the PDF analysis of complex materials.[23] Examination of the PDF through a box-car fitting method (box length of 6 Å, where the centroid of the refinement range is shifted to higher r in 1 Å steps) showed that fitted ratio of LCF-Ta in 0.62[HCF-Sm]·0.38[LCF-Ta] and 0.57[HCF-La]·0.43[LCF-Ta] changed as a function of fitting length scale. The ratio of LCF-Ta rapidly declines at around r_{max} = 9 Å and approaches ≈0 at r_{max} = 18 Å, which confirms the amorphization of LCF-Ta.

The crystalline-amorphous heterostructure of 0.62[HCF-Sm]·0.38[LCF-Ta] particles was further confirmed by HRTEM analysis. The HRTEM image of 0.62[HCF-Sm]·0.38[LCF-Ta] (Figure 2d,e) clearly shows several grains that are spread throughout the particle and interconnected by the amorphous region. Combined XRD and the selected area electron diffraction (Figure S5a, Supporting Information) results, the crystalline regions were identified as HCF-Sm, and its (020) and (011) planes were indicated in Figure 2d. Moreover, the corresponding energy-dispersive spectroscopy (EDS) mapping on the whole particle (Figure S5b, Supporting Information) demonstrates a uniform distribution of Na and Cl elements but a slightly localized distribution of Sm and Ta elements, which further supports that the 0.62[HCF-Sm]·0.38[LCF-Ta] sample is a mixture rather than a solid solution.

To distinguish the Na^+ diffusion of different components, we studied the low-temperature electrochemical impedances of 0.62[HCF-Sm]·0.38[LCF-Ta], HCF-Sm, and LCF-Ta. The LCF-Ta presents a symmetric impedance semicircle (Figure S6a, Supporting Information) at −70 °C, whereas both HCF-Sm (Figure S6b, Supporting Information, 5 °C) and 0.62[HCF-Sm]·0.38[LCF-Ta] (Figure 2f, −70 °C) present an asymmetric impedance semicircle. By fitting the impedance result of 0.62 HCF-Sm·0.38 LCF-Ta, the origins of ionic conductivity were differentiated as the bulk-phase HCF-Sm, amorphous LCF-Ta, and interface/grain boundaries according to the capacitances from low to high, as depicted in Figure 2g.[24] The ionic diffusions in these three regions exhibit a remarkable enhancement when compared to those observed in pristine HCF-Sm or LCF-Ta. Thus, the study of synergistic ion conduction among the crystalline region, the amorphous region, and the interface between crystalline and amorphous warrants thorough investigation.

2.2. The Synergistic Effect Enabled by Heterogenization

To decipher the ion transport in the complex system of HSEs, we began by individually considering the impacts of the crystalline region, the amorphous region, and the interface. Previous studies have examined the space charge layer effect at interfaces[12,25] and the diffusion mechanism in UCl_3-type frameworks.[21,22] Here, we employ simulations to evaluate the influence of amorphous LCF-Ta on Na^+ diffusion. To generate the amorphous structure, we conduct thermal quenching of the crystalline LCF-Ta at temperatures of 1200 and 2000 K and obtain two amorphous structures with increased disordering (**Figure 3**a-c). While Ta-Cl remains local octahedral configurations in the amorphous structures, a notable change in Ta cation ordering is observed in amorphous LCF-Ta, leading to the diverse local environment of Na^+ sites (as illustrated in Figure 3d and Figure S7, Supporting Information). The disordering of the $[TaCl_6]^-$ framework was further illustrated by the calculated radial distribution functions as shown in Figure 4a,b, and the continuous symmetry measure (CSM) analysis suggests stronger distortion of the $[TaCl_6]^-$ octahedrons in amorphous LCF-Ta (Figure 4c, 2000 K-quenched

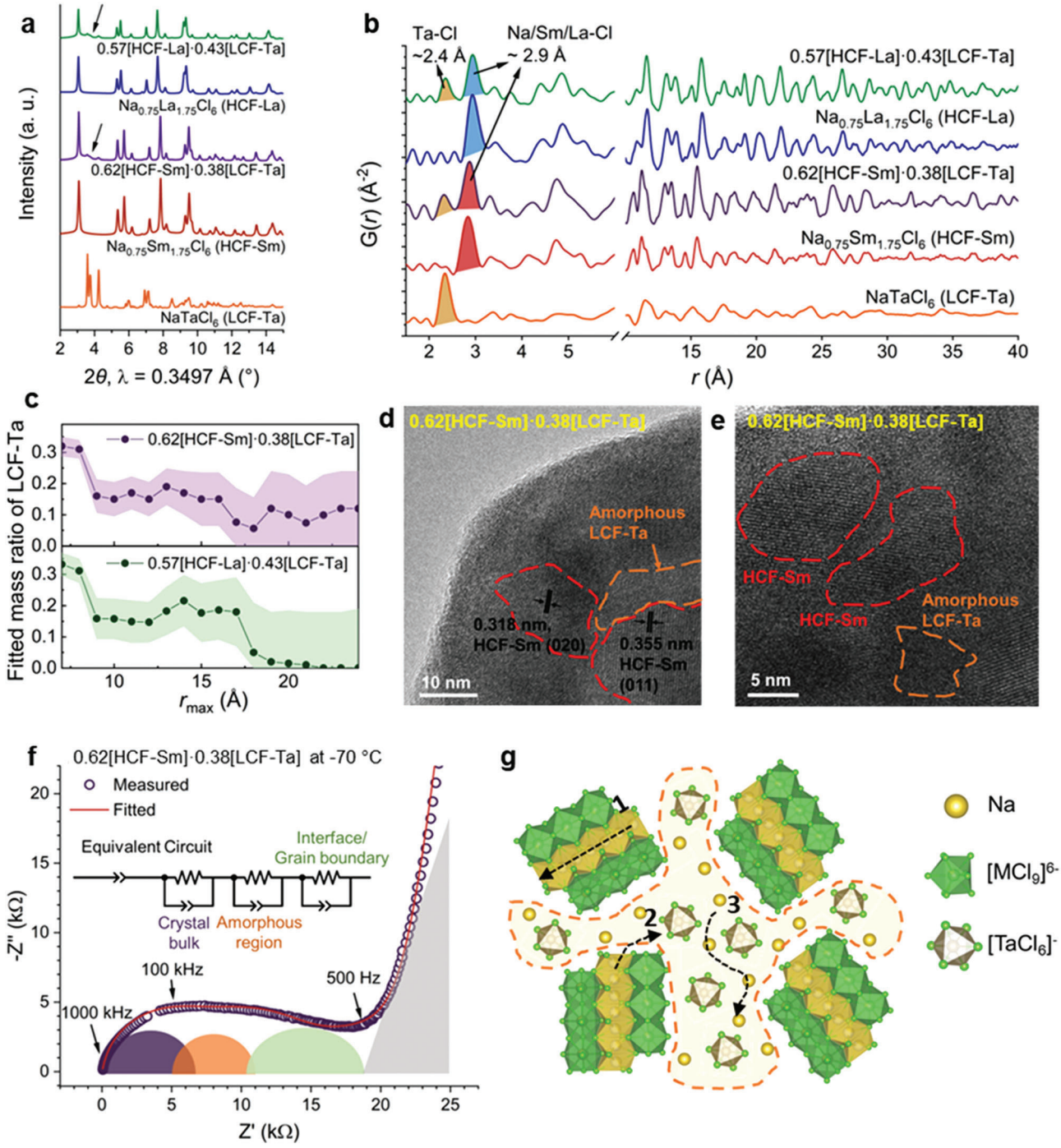

Figure 2. Crystalline-amorphous heterogeneous structures and enhanced ionic conductivities. a) The SXRD patterns (λ = 0.3497 Å) and b) PDFs (λ = 0.1905 Å) of LCF-Ta, HCF-La, HCF-Sm, 0.62[HCF-Sm]·0.38[LCF-Ta], and 0.57[HCF-La]·0.43[LCF-Ta]. c) The fitted mass ratio of LCF-Ta in 0.62[HCF-Sm]·0.38[LCF-Ta], and 0.57[HCF-La]·0.43[LCF-Ta] verse r_{max} from the box-car fitting method. d,e) The HRTEM image taken from the particle edge of 0.62[HCF-Sm]·0.38[LCF-Ta]. f) The electrochemical impedance plot of 0.62[HCF-Sm]·0.38[LCF-Ta] at −70 °C. g) The schematic diagram of heterogeneous halide composites.

>1200K-quenched > Pristine), which is correlated with ionic conductivity as shown in Figure 3e. According to the mechanism of ion diffusion in frustration as illustrated,[26] the Na^+ hopping between these disordered sites has reduced barriers, thus enhancing the ionic conductivity as shown in AIMD simulations (Figure 3e, 2000 K-quenched > 1200 K-quenched > Pristine).

EXAFS is a technique that enables the analysis of local structural information around a specific element absorber, making it an ideal tool for investigating the local coordination of

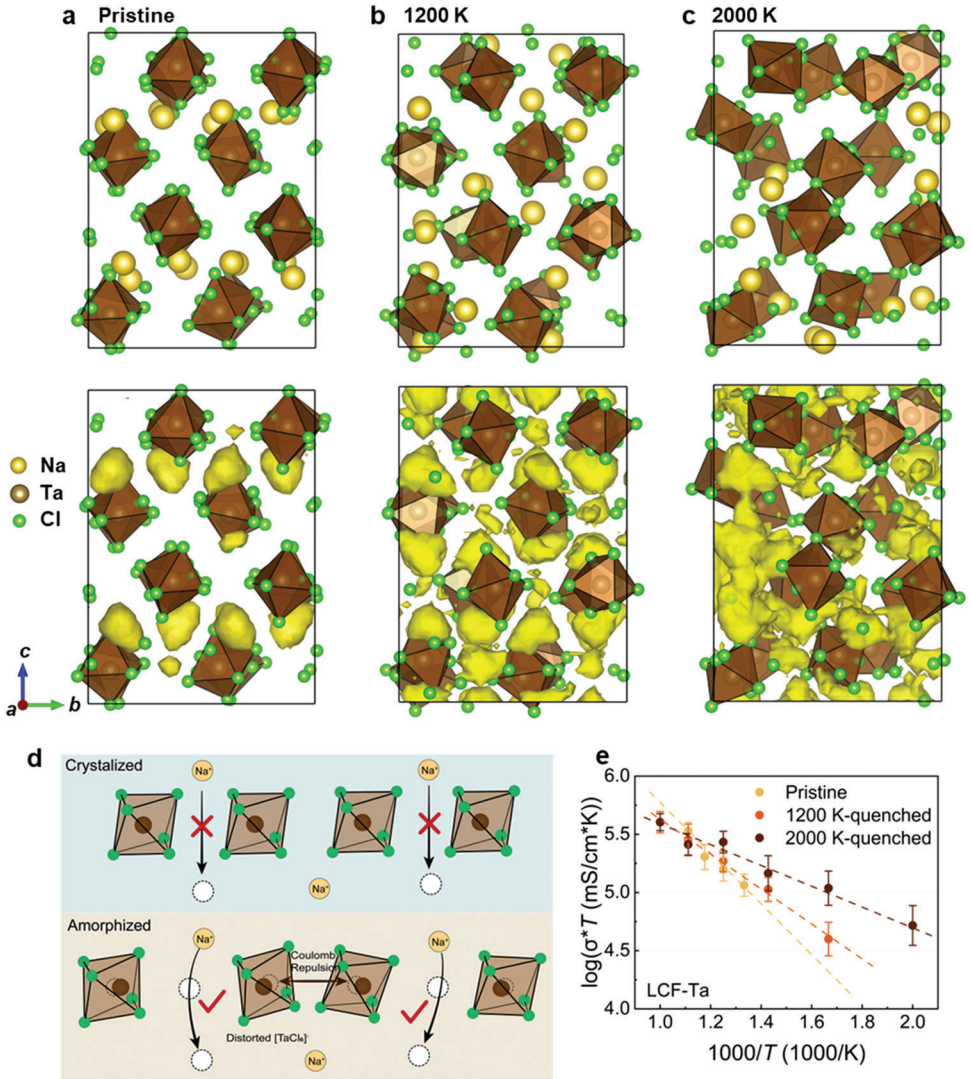

Figure 3. The effect of amorphization of LCF-Ta. Structures of a) pristine LCF-Ta, b) 1200 K-quenched LCF-Ta, and c) 2000 K-quenched LCF-Ta. Below is the Na^+ probability density marked by yellow isosurfaces from AIMD simulations at 700 K. d) Schematics of Na^+ diffusion in crystal versus amorphized LCF-Ta. (e) Arrhenius plot of Na^+ conductivity of crystalline LCF-Ta, 1200 K-quenched LCF-Ta, and 2000 K-quenched LCF-Ta.

specific elements in complex systems. The Fourier-transformed (FT) k^2-weighted $\chi(k)$ of Ta L_3-edge EXAFS spectra of LCF-Ta, 0.62[HCF-Sm]·0.38[LCF-Ta], and 0.57[HCF-La]·0.43[LCF-Ta] are present in **Figure 4**d. The backscattering signals from the first shell of Ta atoms settle at $R = 2.4$ Å (after phase correction) in LCF-Ta, 0.62[HCF-Sm]·0.38[LCF-Ta], and 0.57[HCF-La]·0.43[LCF-Ta], consistent with the Ta-Cl distance obtained from the PDF analysis. Similarly, the Sm L_3-edge EXAFS spectra of 0.62[HCF-Sm]·0.38[LCF-Ta] demonstrate only one characteristic peak located at $R = 2.8$ Å in Figure S8d (Supporting Information), which is identical to that of HCF-Sm and should be ascribed to the backscattering from Cl^- coordination in $[SmCl_9]^{6-}$ tricapped trigonal prisms. This excludes the probability that Ta and Sm are partially displacing each other in the mixture of LCF-Ta and HCF-Sm. Further, in the multiple-scattering region of Figure 4d and Figure S9 (Supporting Information), the focused hinge paths (Ta-Cl-Ta-Cl-Ta at $R > 4$ Å) are very sensitive to the bond angle of Cl-Ta-Cl as depicted in Figure 4e,f (the closer to 180°, the stronger). After further differentiation of scattering signs in k-space (Figure 4g-i), the peak intensity of *f1* at $k = 6$ Å^{-1} and $R = 4.2$ Å can be viewed as a criterion of distortion of $[TaCl_6]^-$ octahedrons. Following the amorphization of LCF-Ta in the heterostructure, we observe a notable increase in the distortion of $[TaCl_6]^-$ octahedrons. This distortion causes a deviation of the central Ta atom, as evidenced by the decrease in the intensity of *f1* in the heterostructure (Figure 4i) compared to pristine LCF-Ta (Figure 4h). The distorting tendency strongly corroborates with our computational simulations, revealing notable alterations in the local environment of Ta within LCF-Ta.

Based on the analysis of the amorphous region, the interplay between the three regions in halide HSEs can be summarized as follows: the LCF-Ta transitions into an amorphous state characterized by disordered $[TaCl_6]^-$ octahedrons when

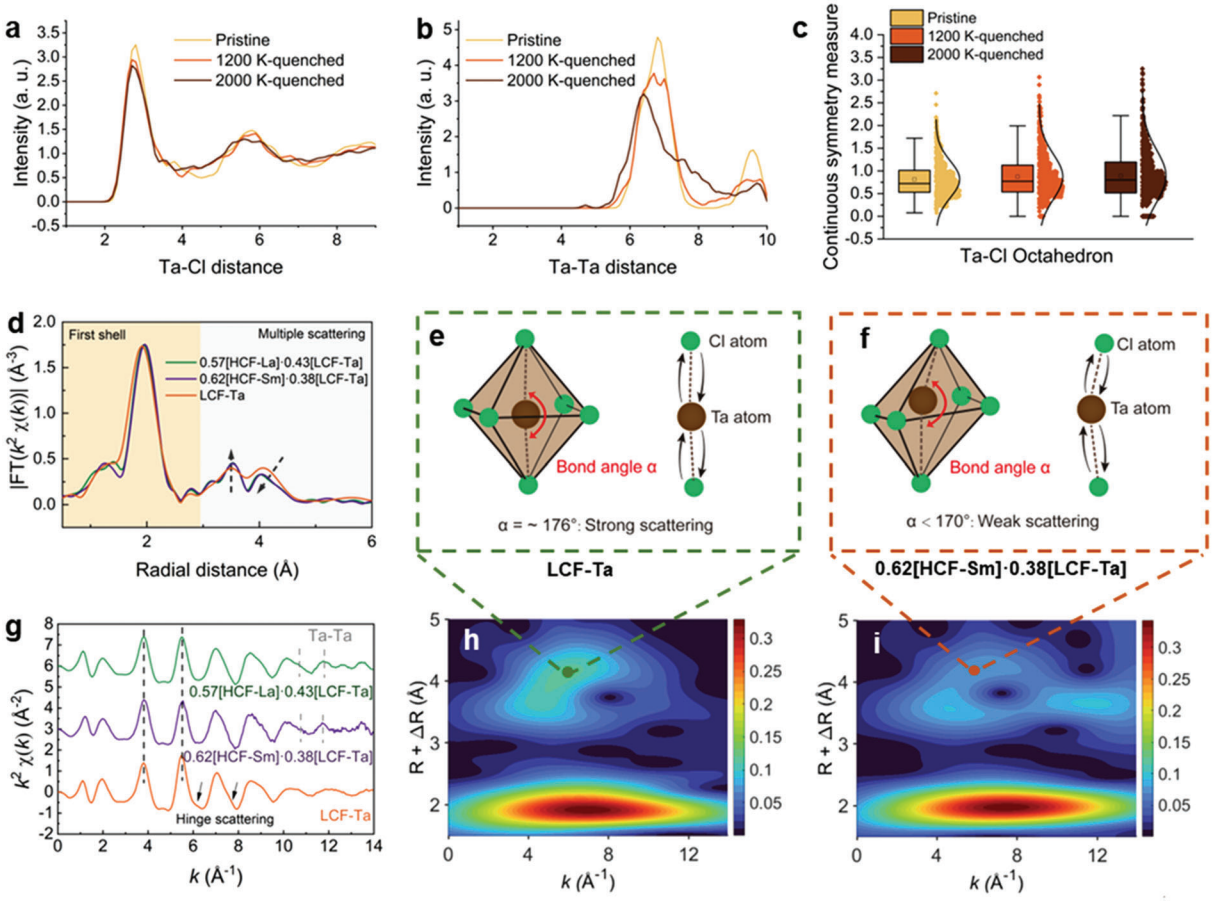

Figure 4. Local distortion in the amorphous LCF-Ta. Calculated radial distribution functions of a) Ta-Cl distance and b) Ta–Ta distance of LCF-Ta. c) The CSM of Ta–Cl Octahedra in LCF-Ta. For each box, the centerline marks the median of the data set, the center square marks the mean of the data set, the outer edges mark the first and third quartiles, and the endpoints are either the extrema values or 1.5 times the interquartile range, whichever is smaller. Data are marked individually as diamonds. All the configurations are sampled at constant 2 ps intervals from the snapshots in AIMD simulation at 600 K. d) Fourier transform of the Ta L_3-edge EXAFS in R-space, with a k^2-weighing, of LCF-Ta, 0.62[HCF-Sm]·0.38[LCF-Ta], and 0.57[HCF-La]·0.43[LCF-Ta]. e,f) The schematic of the relationship between bond angle and the intensity of multiple scattering. g) The Ta L_3-edge EXAFS region in k-space of LCF-Ta, 0.62[HCF-Sm]·0.38[LCF-Ta], and 0.57[HCF-La]·0.43[LCF-Ta]. Wavelet transform of the k^2-weighted EXAFS data of h) LCF-Ta and i) 0.62[HCF-Sm]·0.38[LCF-Ta].

forming the heterogeneous interface with the UCl_3-type framework (i.e., HCFs); the disorder of $[TaCl_6]^-$ octahedrons leads to the diverse local environments around the Na^+ sites with enhanced Na^+ ionic conductivity. These inter-grain amorphous regions then play a critical role in connecting different UCl_3-type frameworks, enabling long-range Na^+ conduction across the HCF grains and the amorphous LCF regions. The heterogeneous interface makes a substantial contribution to the overall ionic conductivity. However, comprehending and simulating this interface presents significant challenges, which will be the focus of our future research. Overall, the three regions synergistically enhanced the ionic conduction via the heterogenization of halide HSEs.

2.3. The SSSB Performance Using Halide HSEs

In addition to their excellent ionic conductivity compared to other halide electrolytes, halide HSEs also possess favorable properties such as deformability and exceptional high-voltage stability. The deformability of solid electrolytes (SEs) can be directly assessed by examining the relative porosity of cold-pressed pellets under a specific pressure. We pressed the electrolyte powders into a pellet under ≈400 MPa. The cross-sectional morphologies of these pellets were examined by scanning electron microscopy (SEM). As depicted in Figure S10 (Supporting Information), pores and voids are clearly observed in high-magnification images of Na_3PS_4 but absent in halide HSEs. The estimated relative density of 0.62[HCF-Sm]·0.38[LCF-Ta], 0.57[HCF-La]·0.43[LCF-Ta], and Na_3PS_4 from SEM results are 92.2%, 89.4%, and 75.2%, respectively, indicating that HSEs has better processibility than the typical sulfide SSC of Na_3PS_4.

The thermodynamic electrochemical windows (vs. Na/Na^+) of HCF-Sm, HCF-La, LCF-Ta, and Na_3PS_4 were calculated using the grand potential phase diagram approach (**Figure 5**a). The stable electrochemical windows were determined as 0.64–4.25 V for HCF-Sm and 0.41–3.76 V for HCF-La, respectively. LCF-Ta has a similar oxidation limit of 3.91 V but a high

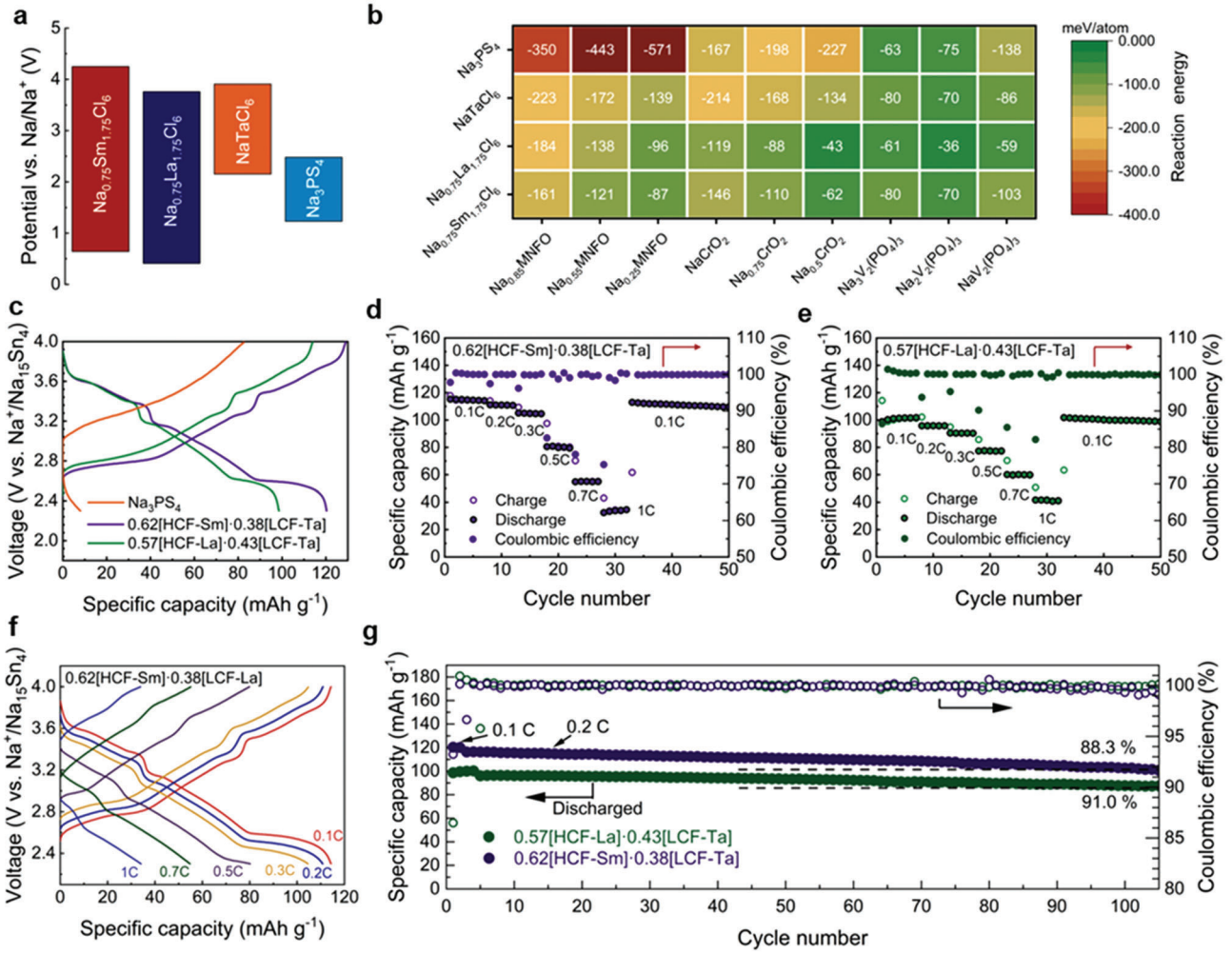

Figure 5. Electrochemical stability and battery performance. a) The calculated stable electrochemical window of different SEs. b) Thermodynamic calculation of decomposition energies between SEs and cathode materials at sodiated and de-sodiated states. c) The 1st charge/discharge profile of cells in which 0.62[HCF-Sm]·0.38[LCF-Ta], 0.57[HCF-La]·0.43[LCF-Ta], or Na_3PS_4 is used as catholyte at RT and 0.1 C (1 C = 120 mAh g^{-1}). d,e) the rate performance of cells using 0.62[HCF-Sm]·0.38[LCF-Ta] and 0.57[HCF-La]·0.43[LCF-Ta] as catholyte at RT. f) The charge/discharge curves of the cell in (d) at various current densities. g) The long cycle performance of cycled between 2.3–4 V vs. Na^+/Na at 0.2 C at 25 °C.

reduction limit of 2.15 V due to the reduction of Ta^{5+}. Overall, halide SSCs generally demonstrate higher oxidation limits than sulfides, such as Na_3PS_4 (1.21 – 2.12 V). The experimental electrochemical windows of 0.62[HCF-Sm]·0.38[LCF-Ta] and 0.57[HCF-La]·0.43[LCF-Ta] are measured using linear sweep voltammetry (LSV) analyses. Matching with theoretical prediction results, 0.62[HCF-Sm]·0.38[LCF-Ta] has a higher oxidation limit than that of 0.57[HCF-La]·0.43[LCF-Ta] (Figure S11, Supporting Information).

The chemical andelectrochemical stabilities between LCF-Ta and other SSCs and various cathode materials were further evaluated by computation.[27] Figure 5b and Tables S5–S8 (Supporting Information) depict the reaction energy and decomposition products between SSCs and cathode materials including NMNFO, $NaCrO_2$, and $Na_3V_2(PO_4)_3$. The de-sodiation of these three cathode materials notably results in instability in contact with Na_3PS_4. Conversely, halide SSCs show greater stability as the Na content decreases. As the options of metal elements for halide HSEs are versatile (e.g., Sm/La and Ta/Zr/Hf) without significantly compromising the high ionic conductivity of the electrolyte, the electrochemical window of halide HSEs and composition of CEI are tunable.

As a proof of concept, the compatibility between different halide HSEs and cathode active materials was studied in SSSBs. A Na_3PS_4 interlayer was inserted between the HSEs and the $Na_{15}Sn_4$ alloy anode. NMNFO was selected as a representative cathode material due to its appropriate operating voltage up to 4 V. Figure 5c presents the initial charge–discharge curves of NMNFO-based SSSBs using different electrolytes at 0.1 C (1 C = 120 mAh g^{-1}). As a control experiment, the cell using only Na_3PS_4 as the electrolyte showed little discharge capacity after being charged to 4 V. In sharp contrast, the cells using either 0.62[HCF-Sm]·0.38[LCF-Ta] or 0.57[HCF-La]·0.43[LCF-Ta] exhibited a reversible charge–discharge process. The interfacial reaction between different electrolytes and NMNFO was investigated by X-ray photoelectron spectroscopy (XPS). As indicated

in Figure S12a,b (Supporting Information) for the cell using Na_3PS_4, both S *2p* and P *2p* XPS spectra exhibited strong signals from P_2S_5 and bridging sulfur (P-[S]$_n$-P), indicating a severe decomposition of Na_3PS_4 at 4 V, and this result is consistent with previous reports on electrodes using Na_3PS_4.[8] As for the cells using halide HSEs, marginal changes of Sm *3d*, La *3d*, Ta *4f*, and Cl *2p* spectra were observed after being charged to 4 V (Figure S12c–h, Supporting Information), confirming the exceptional cationic stability of 0.62[HCF-Sm]·0.38[LCF-Ta] and 0.57[HCF-La]·0.43[LCF-Ta] compared to that of Na_3PS_4. As we have exhibited above, the electrochemical performance of HSEs is far superior to that of Na_3PS_4 when charging the cell to 4 V vs. Na/Na^+.

The rate and cycle performance of cells using 0.62[HCF-Sm]·0.38[LCF-Ta] or 0.57[HCF-La]·0.43[LCF-Ta] are comparable, as depicted in Figure 5d–g. Specifically, the 0.57[HCF-La]·0.43[LCF-Ta] cell showed capacity retention of 91.0% after 100 cycles at 0.2 C, which is slightly higher than the 0.62[HCF-Sm]·0.38[LCF-Ta] cell (88.3%). To be noted, the observed performance at high rates is mainly limited by the poor ionic conductivity of the interlayer Na_3PS_4 (≈0.1 mS cm^{-1}). While the ionic conductivities of 0.62[HCF-Sm]·0.38[LCF-Ta] and 0.57[HCF-La]·0.43[LCF-Ta] are comparable, the discharge capacity and Coulombic efficiency (CE) in the initial cycle is higher when using 0.62[HCF-Sm]·0.38[LCF-Ta] than using 0.57[HCF-La]·0.43[LCF-Ta] (≈117.9 mAh g^{-1} vs. ≈95.1 mAh g^{-1}; 96.1% vs. 85.8%). This can be attributed to the higher oxidation limit of 0.62[HCF-Sm]·0.38[LCF-Ta] due to the use of HCF-Sm instead of HCF-La. Recent research has shown the critical role of metal elements in halide electrolytes in determining the high-voltage stability of the battery.[28] Within HSEs, the choice of components also affects the performance of the battery as the 0.62[HCF-Sm]·0.38[LCF-Ta] cell delivered higher discharge capacity whereas the 0.57[HCF-La]·0.43[LCF-Ta] cell exhibited better cycle performance.

3. Conclusion

In summary, our findings lead to a novel class of halide HSEs by utilizing the synergistic effect between high- and low-coordination halide frameworks, demonstrating comprehensive advantages of high ionic conductivity, excellent high-voltage stability, and deformability. The optimized 0.62[HCF-Sm]·0.38[LCF-Ta] and 0.57[HCF-La]·0.43[LCF-Ta] HSEs exhibited a remarkable RT Na^+ conductivity of 2.7 and 1.8 mS cm^{-1}, respectively, which are among the highest values reported so far for halide SSCs. The diffusion mechanism in this class of halide HSEs was studied, revealing distinct contributions from crystalline bulk, amorphous region, and the heterogeneous interface between them. In particular, the effect of amorphized components in HSEs was studied. The amorphization process significantly increases the ionic conductivity of target components and assists in establishing connections between discrete UCl_3-type framework particles, thereby enabling fast long-range Na^+ conduction across the macroscopic HSEs. With good deformability and high-voltage stability of HSEs, direct integration with NMNFO cathode can be achieved by simple cold-pressing to demonstrate a stable cathode/catholyte interface and a capacity retention of 91.0% after 100 cycles at 0.2 C for SSSBs. In addition, a theoretical study of interfacial reactions between SSCs and cathode materials revealed different interfacial products upon the choice of SSCs and cathode materials. The component in HSEs is versatile, allowing for a tunable CEI design for different cathode materials. Owing to the comprehensive advantages, the heterogeneous halide composite SSC is an ideal choice for achieving high-performance SSSBs.

4. Experimental Section

DFT Calculation: All density functional theory (DFT) calculations were performed using Vienna Ab initio Simulation package (VASP)[29] within the projector augmented-wave (PAW) approach[30] and Perdew–Burke–Ernzerhof (PBE) generalized-gradient approximation (GGA) functional.[31] The convergence parameters in static DFT calculations were consistent with the Materials Project.[32]

Generation of Amorphous Structures: The supercell models of crystal $NaTaCl_6$ (a total of 128 atoms) were heated from 100 K to target temperature (1200 and 2000 K) at a constant rate within a period of 2 ps and then equilibrated for 20 ps. Finally, the configurations were quenched to 100 K at a constant rate within a period of 2 ps. In all simulations, non-spin-polarized mode, a time step of 2 fs, and NVT ensemble using a Nose´-Hoover thermostat[33] were used.

Ab Initio Molecular Dynamics (AIMD) Simulations: To investigate ionic diffusion, AIMD simulations were performed on the supercell models of HCF-SM (a total of 68 atoms), HCF-LA (a total of 68 atoms), and LCF-TA (a total of 128 atoms). Non-spin-polarized mode and a Γ-centered k-point were used. A time step of 2 fs and NVT ensemble using a Nose´-Hoover thermostat[33] was used in all simulations. The structures were heated from 100 K to the targeted temperature (400–1000 K) at a constant rate during a period of 2 ps. The D was calculated as the mean square displacement (MSD) over the time interval Δt:

$$D = \frac{1}{2Nd\Delta t} \sum_{i=1}^{N} \left\langle [r_i(t + \Delta t) - r_i(t)]^2 \right\rangle_t \quad (1)$$

The ionic conductivity was calculated according to the Nernst–Einstein relationship:

$$\sigma = \frac{nq^2}{k_B T} D \quad (2)$$

where n is the mobile ions volume density and q is the ionic charge. The activation energy and ionic conductivity at the desired temperature were extrapolated according to the Arrhenius relation:

$$\sigma T = \sigma_0 \exp\left(\frac{-E_a}{k_B T}\right) \quad (3)$$

where E_a is the activation energy, σ_0 is the pre-exponential factor. The statistical deviation of the diffusivity was evaluated using the scheme established in previous work,[34] then the simulations lasted 40 to 300 ps until the diffusivity converged within a relative standard deviation of 20–40%. The Na-ion probability density was calculated as the time fraction of Na-ions at each spatial location in the crystal structures during the AIMD simulations. The demonstration of crystal structure was performed by VESTA software.[35]

Thermodynamic Calculations of Interface Stabilities: To evaluate the interfacial stability between SE and common cathode materials, the interface pseudo-binary reaction energy was calculated as:

$$\Delta E_D(\text{SE, cathode}, x) = E_{eq}(C_{interface}(C_{SE}, C_{cathode}, x)) - E_{interface}(\text{SE, cathode}, x) \quad (4)$$

where C_{SE} and $C_{cathode}$ are the compositions of SE and cathode materials, normalized to one atom per formula. The x is the molar fraction of the SE.

The energies of materials were obtained from Material Project database. More details can be found in previous studies.[36]

Thermodynamic Calculations of Electrochemical Window: The electrochemical window was evaluated using the method in our previous studies.[36a,37] A grand potential phase diagram was used to identify the phase equilibria of a given phase in equilibrium with the Na reservoir at chemical potential μ_{Na} referenced to N_a metal. The stable electrochemical window of the phase was estimated as the range of μ_{Na}, where the phase is neither oxidized nor reduced.

Synthesis Methods: All preparation processes and sample treatments were carried out in an Ar-filled glovebox (O_2 < 1 ppm, H_2O < 1 ppm). The UCl_3-type halides HCF-Sm/HCF-La and ternary halides $NaTaCl_6$, Na_2ZrCl_6, and Na_2HfCl_6 were synthesized by ball-milling the starting materials of NaCl (Sigma Aldrich, 99.9% purity), $SmCl_3$ (Sigma Aldrich, 99.9% purity) and $LaCl_3$ (Sigma Aldrich, 99.8% purity), $TaCl_5$ (Sigma Aldrich, 99.99% purity), $ZrCl_4$ (Sigma Aldrich, 99.9% purity), and $HfCl_4$ (Sigma Aldrich, 99.9% purity) at the stated stoichiometric ratio. For ball-milling synthesis, the mixture of precursors was sealed in a zirconia jar (100 mL) under vacuum and ball-milled at 500 rpm for 60 cycles. Each cycle included 10-min milling and 5-min resting. The heterogeneous composite was synthesized by ball-milling as-prepared HCF-Sm/HCF-La and $NaTaCl_6$/Na_2ZrCl_6/Na_2HfCl_6 at 500 rpm for another 20 cycles or directly from the precursors at 500 rpm for 90 cycles.

Characterization: Lab-based XRD measurements were performed on Bruker AXS D8 Advance with Cu Kα radiation (λ = 1.5406 Å). Kapton tape was used to cover the sample holder to prevent air exposure. SEM images and element mappings were obtained by using a Hitachi S-4800 field-emission scanning electron microscope (FE-SEM, acceleration voltage 5 kV) equipped with EDS. The HRTEM images, EDS mapping, and selected area electron diffraction patterns of the studied samples were performed by a Cs-corrected Titan Themis 80–300 TEM, operated at 300 kV, fitted with a Bruker Quantax Super-X EDS detector. The sample powder was directly dispersed on a Cu grid without the assistance of solvent. Elemental maps were acquired at a beam current of 200 pA and an acquisition time of 10–15 min. A standard-based quantification method (Linemarker TEM) was used for the elemental quantification of the acquired elemental maps.

The SXRD and PDF were collected using the Brockhouse High Energy Wiggler beamline at the Canadian Light Source (CLS) with a wavelength of 0.3497 Å. The samples were loaded into 0.8 mm inner diameter polyimide capillaries and sealed with epoxy in an Ar-filled glove box. The X-ray diffraction Rietveld refinement and pair distributed function fittings were conducted by GSAS-2 and PDFgui software.[38] X-ray absorption spectra (XAS) were collected from the Hard X-ray Micro-Analysis (HXMA) and soft X-ray micro characterization (SXRMB) beamlines of CLS, the samples were mixed with BN and pressed into pellets to achieve an absorption length of 1. Samples for Cl K-edge were spread on carbon tape and measured within a vacuum chamber. All XAS data were analyzed with the Athena software, and the EXAFS data were processed using the Artemis program.[39]

Electrochemical Characterizations: The temperature-dependent ionic conductivities of prepared SEs were obtained via the EIS measurements of model cells on a multichannel potentiostat 3/Z (German VMP3). The applied frequency range was 1 Hz to 7 MHz and the voltage amplitude was 20 mV. The test cell was fabricated by pressing electrolytes into a pellet (≈400 MPa, 120 mg samples, diameter of 1 cm, thickness ≈0.5–0.6 mm). About 5 mg of acetylene black carbon was then spread onto both sides of the pellet and pressed with ≈150 MPa.

The model SSSB was assembled by using the NMNFO as the cathode, Na-Sn (15:4) as the negative electrode, and halide HSEs and/or Na_3PS_4 as the separator (see diagram of battery architecture in Figure S11, Supporting Information). A total of 100 mg of the electrolyte powder to be tested was pressed at ≈200 MPa to form an SE layer (1 cm diameter). The cathode composite (NMNFO: SSC: carbon black (CB) = 60:40:2) was uniformly spread onto the surface of one side of the electrolyte layer and pressed with ≈400 MPa for 1 min. Then about 7 mg of the cathode composite was placed on one side of the SSC pellet and pressed at the same pressure, and on the opposite side of SSC, the Na_3PS_4, and an excess of Na-Sn alloy (60 mg) were pressed in order. Galvanostatic charge–discharge for SSSB was conducted on the LAND battery test system (CT3002AU-5V10mA) at RT with a stack pressure of ≈80 MPa. The LSV measurement used the same configuration except that the cathode composite was replaced by the mixed powder of the SSC and CB in a weight ratio of 9:1 using a mortar and a pestle. The scan ranges from the open-circuit voltage (OCV) to 6 V (vs. Na/Na^+, positive scan) or OCV to 0 V (vs. Na/Na^+, negative scan), respectively. The scan rate was 0.1 mV s^{-1}.

Supporting Information

Supporting Information is available from the Wiley Online Library or from the author.

Acknowledgements

The authors thank the support from the Natural Sciences and Engineering Research Council of Canada (NSERC), the Canada Research Chair Program (CRC), the Canada Foundation for Innovation (CFI), and Western University. The synchrotron-related characterizations were completed at the HXMA, SXRMB, and BXDS beamline in Canadian Light Source (CLS), which is supported by the Canada Foundation for Innovation (CFI), the Natural Sciences and Engineering Research Council (NSERC), the National Research Council (NRC), the Canadian Institutes of Health Research (CIHR), the Government of Saskatchewan, and the University of Saskatchewan. M.G. wants to acknowledge the support from Guangdong Fundamental Research Association with the project no. 2022B1515120013, National Natural Science Foundation of China (52273225), Guangdong scientific program with contract no. 2019QN01L057. Y.M. acknowledges the funding support from National Science Foundation Award# 2118838 and the computational facilities from the University of Maryland supercomputing resources.

Conflict of Interest

The authors declare no conflict of interest.

Author Contributions

J.F., S.W., and D.W. contributed equally to this work. J.F. and S.W. conceived the project. J.F. performed the electrolyte synthesis and characterization. S.W. performed the computational simulations. D.W. conducted TEM measurements and analyses under the supervision of M.G. X.L. helped with the fabrication of SSSBs. C.W. and J.L. contributed to the experiment design and data analysis. Y.H., S.Z., F.Z., W.L., and M.L. helped with synchrotron-related characterizations. H.D. and Y.Z. conducted the SEM and XRD measurements. J.F., S.W., D.W., and J.L. formally analyzed all data and wrote the manuscript. M.G., T.K.S., Y.M., and X.S. supervised the project. All the authors participated in the reviewing and editing of the manuscript.

Data Availability Statement

The data that support the findings of this study are available from the corresponding author upon reasonable request.

Keywords

composites, heterogeneous structure, Na^+ diffusion, solid-state electrolyte, UCl_3-type framework

Received: August 8, 2023
Revised: October 9, 2023
Published online: November 30, 2023

[1] a) H.-L. Yang, B.-W. Zhang, K. Konstantinov, Y.-X. Wang, H.-K. Liu, S.-X. Dou, *Adv. Energy Sustainability Res.* **2021**, *2*, 2000057; b) C. Vaalma, D. Buchholz, M. Weil, S. Passerini, *Nat. Rev. Mater.* **2018**, *3*, 18013; c) J.-Y. Hwang, S.-T. Myung, Y.-K. Sun, *Chem. Soc. Rev.* **2017**, *46*, 3529.
[2] a) Y.-K. Sun, *ACS Energy Lett.* **2020**, *5*, 3221; b) A. M. Abakumov, S. S. Fedotov, E. V. Antipov, J. M. Tarascon, *Nat. Commun.* **2020**, *11*, 4976; c) N. Zhao, W. Khokhar, Z. Bi, C. Shi, X. Guo, L.-Z. Fan, C.-W. Nan, *Joule* **2019**, *3*, 1190.
[3] a) Y.-F. Y. Yao, J. Kummer, *J. Inorg. Nucl. Chem.* **1967**, *29*, 2453; b) J. B. Goodenough, H.-P. Hong, J. Kafalas, *Mater. Res. Bull.* **1976**, *11*, 203.
[4] A. Gigante, L. Duchêne, R. Moury, M. Pupier, A. Remhof, H. Hagemann, *ChemSusChem* **2019**, *12*, 4832.
[5] a) A. Hayashi, K. Noi, A. Sakuda, M. Tatsumisago, *Nat. Commun.* **2012**, *3*, 856; b) S. Takeuchi, K. Suzuki, M. Hirayama, R. Kanno, *J. Solid State Chem.* **2018**, *265*, 353.
[6] a) X. Feng, P. H. Chien, Z. Zhu, I. H. Chu, P. Wang, M. Immediato-Scuotto, H. Arabzadeh, S. P. Ong, Y. Y. Hu, *Adv. Funct. Mater.* **2019**, *29*, 1807951. b) I. H. Chu, C. S. Kompella, H. Nguyen, Z. Zhu, S. Hy, Z. Deng, Y. S. Meng, S. P. Ong, *Sci. Rep.* **2016**, *6*, 33733; c) A. Hayashi, N. Masuzawa, S. Yubuchi, F. Tsuji, C. Hotehama, A. Sakuda, M. Tatsumisago, *Nat. Commun.* **2019**, *10*, 5266; d) A. Banerjee, K. H. Park, J. W. Heo, Y. J. Nam, C. K. Moon, S. M. Oh, S. T. Hong, Y. S. Jung, *Angew. Chem., Int. Ed. Engl.* **2016**, *128*, 9786; e) S.-H. Bo, Y. Wang, J. C. Kim, W. D. Richards, G. Ceder, *Chem. Mater.* **2015**, *28*, 252; f) T. Krauskopf, C. Pompe, M. A. Kraft, W. G. Zeier, *Chem. Mater.* **2017**, *29*, 8859.
[7] a) X. Li, J. Liang, N. Chen, J. Luo, K. R. Adair, C. Wang, M. N. Banis, T. K. Sham, L. Zhang, S. Zhao, S. Lu, H. Huang, R. Li, X. Sun, *Angew. Chem., Int. Ed. Engl.* **2019**, *58*, 16427; b) X. Li, J. Liang, J. Luo, M. Norouzi Banis, C. Wang, W. Li, S. Deng, C. Yu, F. Zhao, Y. Hu, T.-K. Sham, L. Zhang, S. Zhao, S. Lu, H. Huang, R. Li, K. R. Adair, X. Sun, *Energy Environ. Sci.* **2019**, *12*, 2665; c) L. Zhou, C. Y. Kwok, A. Shyamsunder, Q. Zhang, X. Wu, L. F. Nazar, *Energy Environ. Sci.* **2020**, *13*, 2056; d) J. Liang, X. Li, S. Wang, K. R. Adair, W. Li, Y. Zhao, C. Wang, Y. Hu, L. Zhang, S. Zhao, S. Lu, H. Huang, R. Li, Y. Mo, X. Sun, *J. Am. Chem. Soc.* **2020**, *142*, 7012; e) K. Wang, Q. Ren, Z. Gu, C. Duan, J. Wang, F. Zhu, Y. Fu, J. Hao, J. Zhu, L. He, C. W. Wang, Y. Lu, J. Ma, C. Ma, *Nat. Commun.* **2021**, *12*, 4410; f) H. Kwak, D. Han, J. Lyoo, J. Park, S. H. Jung, Y. Han, G. Kwon, H. Kim, S. T. Hong, K. W. Nam, Y. S. Jung, *Adv. Energy Mater.* **2021**, *11*, 2003190; g) T. Asano, A. Sakai, S. Ouchi, M. Sakaida, A. Miyazaki, S. Hasegawa, *Adv. Mater.* **2018**, *30*, 1803075; h) R. Schlem, S. Muy, N. Prinz, A. Banik, Y. Shao-Horn, M. Zobel, W. G. Zeier, *Adv. Energy Mater.* **2019**, *10*, 1903719; i) J. Fu, S. Wang, J. Liang, S. H. Alahakoon, D. Wu, J. Luo, H. Duan, S. Zhang, F. Zhao, W. Li, *J. Am. Chem. Soc.* **2022**, *145*, 2183.
[8] H. Kwak, J. Lyoo, J. Park, Y. Han, R. Asakura, A. Remhof, C. Battaglia, H. Kim, S.-T. Hong, Y. S. Jung, *Energy Storage Mater.* **2021**, *37*, 47.
[9] R. Schlem, A. Banik, M. Eckardt, M. Zobel, W. G. Zeier, *ACS Appl. Energy Mater.* **2020**, *3*, 10164.
[10] E. A. Wu, S. Banerjee, H. Tang, P. M. Richardson, J. M. Doux, J. Qi, Z. Zhu, A. Grenier, Y. Li, E. Zhao, G. Deysher, E. Sebti, H. Nguyen, R. Stephens, G. Verbist, K. W. Chapman, R. J. Clement, A. Banerjee, Y. S. Meng, S. P. Ong, *Nat. Commun.* **2021**, *12*, 1256.
[11] P. Ridley, L. H. B. Nguyen, G. D. E. Sebti, Y.-T. Chen, B. Sayahpour, A. Cronk, G. Deysher, S.-Y. Ham, J. A. S. Oh, E. A. Wu, D. H. S. Tan, J.-M. Doux, R. Clément, J. Jang, Y. S. Meng, *ChemRxiv. Cambridge: Cambridge Open Engage* **2022**.
[12] Z. Zou, Y. Li, Z. Lu, D. Wang, Y. Cui, B. Guo, Y. Li, X. Liang, J. Feng, H. Li, C. W. Nan, M. Armand, L. Chen, K. Xu, S. Shi, *Chem. Rev.* **2020**, *120*, 4169.
[13] H. Kwak, J. S. Kim, D. Han, J. S. Kim, J. Park, G. Kwon, S. M. Bak, U. Heo, C. Park, H. W. Lee, K. W. Nam, D. H. Seo, Y. S. Jung, *Nat. Commun.* **2023**, *14*, 2459.
[14] C. Liang, *J. Electrochem. Soc.* **1973**, *120*, 1289.
[15] S. V. Patel, E. Truong, H. Liu, Y. Jin, B. L. Chen, Y. Wang, L. Miara, R. Kim, Y.-Y. Hu, *Energy Storage Mater.* **2022**, *51*, 88.
[16] M. Tatsumisago, N. Torata, T. Saito, T. Minami, *J. Non-Cryst. Solids* **1996**, *196*, 193.
[17] R. Mercier, J.-P. Malugani, B. Fahys, G. Robert, *Solid State Ionics* **1981**, *5*, 663.
[18] Y. S. Choi, Y.-S. Lee, K. H. Oh, Y. W. Cho, *Phys. Chem. Chem. Phys.* **2016**, *18*, 22540.
[19] C. Tambelli, A. Bloise, A. Rosario, E. Pereira, C. J. Magon, J. P. Donoso, *Electrochim. Acta* **2002**, *47*, 1677.
[20] J. Zheng, M. Tang, Y. Y. Hu, *Angew. Chem., Int. Ed. Engl.* **2016**, *55*, 12538.
[21] J. Fu, S. Wang, J. Liang, S. H. Alahakoon, D. Wu, J. Luo, H. Duan, S. Zhang, F. Zhao, W. Li, M. Li, X. Hao, X. Li, J. Chen, N. Chen, G. King, L.-Y. Chang, R. Li, Y. Huang, M. Gu, T.-K. Sham, Y. Mo, X. Sun, *J. Am. Chem. Soc.* **2023**, *145*, 2183.
[22] Y. C. Yin, J. T. Yang, J. D. Luo, G. X. Lu, Z. Huang, J. P. Wang, P. Li, F. Li, Y. C. Wu, T. Tian, Y. F. Meng, H. S. Mo, Y. H. Song, J. N. Yang, L. Z. Feng, T. Ma, W. Wen, K. Gong, L. J. Wang, H. X. Ju, Y. Xiao, Z. Li, X. Tao, H. B. Yao, *Nature* **2023**, *616*, 77.
[23] X. Qiu, T. Proffen, J. Mitchell, S. Billinge, *Phys. Rev. Lett.* **2005**, *94*, 177203.
[24] J. T. Irvine, D. C. Sinclair, A. R. West, *Adv. Mater.* **1990**, *2*, 132.
[25] a) J. Maier, *Solid State Ionics* **1987**, *23*, 59; b) J. Maier, *J. Electrochem. Soc.* **1987**, *134*, 1524; c) N. Sata, K. Eberman, K. Eberl, J. Maier, *Nature* **2000**, *408*, 946.
[26] S. Wang, Y. Liu, Y. Mo, *Angew. Chem.* **2023**, *135*, e202215544.
[27] a) Y. Zhu, X. He, Y. Mo, *J. Mater. Chem.* **2016**, *4*, 3253; b) A. M. Nolan, Y. Liu, Y. Mo, *ACS Energy Lett.* **2019**, *4*, 2444.
[28] I. Kochetkov, T.-T. Zuo, R. Ruess, B. Singh, L. Zhou, K. Kaup, J. Janek, L. Nazar, *Energy Environ. Sci.* **2022**, *15*, 3933.
[29] G. Kresse, J. Furthmüller, *Phys. Rev. B* **1996**, *54*, 11169.
[30] P. E. Blöchl, *Phys. Rev. B* **1994**, *50*, 17953.
[31] J. P. Perdew, M. Ernzerhof, K. Burke, *J. Chem. Phys.* **1996**, *105*, 9982.
[32] A. Jain, S. P. Ong, G. Hautier, W. Chen, W. D. Richards, S. Dacek, S. Cholia, D. Gunter, D. Skinner, G. Ceder, *APL Mater.* **2013**, *1*, 011002.
[33] N. Shuichi, *Prog. Theor. Phys. Suppl.* **1991**, *103*, 1.
[34] X. He, Y. Zhu, A. Epstein, Y. Mo, *npj Comput. Mater.* **2018**, *4*, 18.
[35] K. Momma, F. Izumi, *J. Appl. Crystallogr.* **2011**, *44*, 1272.
[36] a) Y. Zhu, X. He, Y. Mo, *ACS Appl. Mater. Interfaces* **2015**, *7*, 23685; b) Y. Z. Zhu, X. F. He, Y. F. Mo, *Adv. Sci.* **2017**, *4*, 1600517; c) Y. Z. Zhu, X. F. He, Y. F. Mo, *J. Mater. Chem. A* **2016**, *4*, 3253.
[37] S. Wang, Q. Bai, A. M. Nolan, Y. Liu, S. Gong, Q. Sun, Y. Mo, *Angew. Chem., Int. Ed. Engl.* **2019**, *58*, 8039.
[38] a) B. H. Toby, R. B. Von Dreele, *J. Appl. Crystallogr.* **2013**, *46*, 544; b) C. Farrow, P. Juhas, J. Liu, D. Bryndin, E. Božin, J. Bloch, T. Proffen, S. Billinge, *J. Phys.: Condens. Matter* **2007**, *19*, 335219.
[39] B. Ravel, M. Newville, *J. Synchrotron Radiat.* **2005**, *12*, 537.